ADVANCED MATERIALS
www.advmat.de

Van der Waals Integration of 1D $Nb_2Pd_3Se_8$ and 2D WSe_2 for Gate-Tunable In-Sensor Image Processing

Vu Khac Dat, Minh Chien Nguyen, Byung Joo Jeong, Ngoc Thanh Duong, Van Dam Do, Chengyun Hong, Duong Hai Phuong, Van Tu Vu, Jinsu Kang, Xiaojie Zhang, Robert A. Taylor, Kwangseuk Kyhm, Woo Jong Yu, Jae-Young Choi, and Ji-Hee Kim**

1D and 2D integrations provide significant promise for machine vision by enabling compact, power-efficient optoelectronic devices. However, the potential of 1D materials in mixed-dimensional structures for convolutional image processing remains largely unexplored. Here, high-quality 1D-$Nb_2Pd_3Se_8$ is synthesized and integrated with 2D-WSe_2 to form self-powered photodetectors, exhibiting gate-tunable bi-directional photoresponse for image processing. Utilizing the narrow band gap and favorable work function of 1D-$Nb_2Pd_3Se_8$, a type-I junction and 1D van der Waals interface are established with transition metal dichalcogenides. The gate tunable built-in electric field enables switching between n-p and n-n^+ configurations, allowing the drift photocurrent direction to be reversed, achieving both negative and positive photocurrent. Furthermore, efficient conversion of high-energy photons along one dimension enhances sensitivity at 375 nm. The device achieves a responsivity of 232 mA W^{-1}, external quantum efficiency of 77% at 375 nm illumination, rapid response time of ~3 µs, detectivity of 6.35 × 10^{10} Jones, and broadband photodetection from ultraviolet to near-infrared. The demonstrated gate-controllable, bi-directional photoresponse with linear power dependence in a 1D heterojunction offers a promising platform for in-sensor convolutional processing with high integration and portability.

1. Introduction

Conventional image sensors rely on a physical separation between image sensing and processing, which introduces challenges such as power consumption inefficiency, latency, and increased hardware complexity.[1–5] In-sensor image processing allows for simultaneous visual data acquisition and preliminary processing, making it a promising approach for machine vision applications such as autonomous vehicles, robotics, and environmental analysis.[6–12] Recent advancements in in-sensor optoelectronic computing have demonstrated that implementing edge extraction directly within the front-end photodiode array enhances object tracking and recognition efficiency while improving economic feasibility.[13] This process relies on the use of both positive and negative weights for effective edge extraction, making it a critical requirement for in-sensor image processing.[7,13–15] To meet this

V. K. Dat, N. T. Duong, C. Hong, D. H. Phuong
Department of Energy Science
Sungkyunkwan University
Suwon 16419, Republic of Korea

M. C. Nguyen, V. D. Do, V. T. Vu, W. J. Yu
Department of Electrical and Computer Engineering
Sungkyunkwan University
Suwon 16419, Republic of Korea

B. J. Jeong, J. Kang, X. Zhang, J.-Y. Choi
School of Advanced Materials Science & Engineering
Sungkyunkwan University
Suwon 16419, Republic of Korea
E-mail: jy.choi@skku.edu

The ORCID identification number(s) for the author(s) of this article can be found under https://doi.org/10.1002/adma.202500011

DOI: 10.1002/adma.202500011

R. A. Taylor
Department of Physics
University of Oxford
Oxford OX1 3PU, UK

K. Kyhm
Department of Opto-mechatronics Engineering
Pusan National University
Busan 46241, Republic of Korea

J.-Y. Choi
SKKU Advanced Institute of Nanotechnology (SAINT), and KIST-SKKU Carbon-Neutral Research Center
Sungkyunkwan University
Suwon 16419, Republic of Korea

J.-H. Kim
Department of Physics
Pusan National University
Busan 46241, Republic of Korea
E-mail: kimjihee@pusan.ac.kr

requirement, extensive research has explored various approaches, including ferroelectric-defined sensor arrays,[7] gate-tunable band alignments,[15] and electrostatically doped semiconductors.[2,13] However, these devices face significant design complexity, particularly when employing dual-gate architecture. Moreover, semi-metallic narrow gap materials in heterostructures exhibit inefficient gate-tunable photocarrier collection due to their short photocarrier lifetimes and high dark currents.[16,17] Additionally, while in-sensor image processing offers significant benefits such as power savings, reduced redundant vision data, and increased processing speed, it also comes with certain trade-offs. The complexity of designing efficient analog in-sensor systems that seamlessly integrate sensing and computing remains a significant challenge.[1,18] To overcome these limitations, significant innovations in materials, computing architectures, and scalable device fabrication are essential for advancing in-sensor image processing technologies.

Van der Waals (vdW) heterostructures recently exhibit significant potential in electronic and optoelectronic device applications.[19–26] The integration of mixed-dimensional structures within these heterostructures not only advances fundamental nanoscience research but also enables the development of high-performance nanoscale devices.[27–30] Among these, 2D transition metal dichalcogenides (TMDs) have gained significant attention due to their exceptional optical properties, scalability, and dangling bond-free surfaces, allowing seamless integration with materials of different dimensions.[20–22,27–35] While 2D materials provide excellent tunability and interface compatibility, 1D materials offer unique advantages for charge carrier confinement and efficient transport, particularly in optoelectronic applications. The confined active area in 1D quantum structures enables high charge carrier concentration and directed propagation, making them ideal for achieving high-resolution image sensing.[36–37] Although 1D nanowires have limited light absorption due to their small active area (2–200 nm diameter), this challenge can be mitigated by arranging multiple nanowires side by side, thereby enhancing the light-absorbing area and collection efficiency.[38] By scaling the active region to a 1D heterojunction within 1D/2D mixed-dimensional structures, novel image sensing can be revealed by simultaneously leveraging the unique advantages of both 1D and 2D materials. Recently, 1D ternary vdW materials with a narrow bandgap, excellent scalability, and dangling bonds-free surface have garnered significant attention in advanced optoelectronic devices.[31,39–40] Among them, 1D ternary $Nb_2Pd_3Se_8$ stands out due to its semiconducting behavior, narrow bandgap, air stability, and work function well-aligned with 2D-TMDs such as WSe_2, MoS_2, and $MoSe_2$.[41,42] The $Nb_2Pd_3Se_8$/2D-TMDs heterostructure is particularly advantageous for achieving a unilateral depletion region, which is critical for high-efficiency photovoltaic and optoelectronic devices.[19,43] Despite its promising properties, the potential of 1D-$Nb_2Pd_3Se_8$ in heterostructure-based optoelectronic devices remains largely unexplored.

In this work, we demonstrate a gate-tunable bipolar photoresponse in self-powered photodetectors (V_{DS} = 0 V) based on a 1D-$Nb_2Pd_3Se_8$/2D-TMDs (WSe_2, $MoSe_2$, MoS_2) heterostructure, designed for convolutional image processing. The high-quality $Nb_2Pd_3Se_8$ is synthesized via the chemical vapor transport (CVT) method, and a high-performance $Nb_2Pd_3Se_8$-based photodetector with high responsivity, fast response speed, and broadband photodetection is exhibited. This reveals the potential of $Nb_2Pd_3Se_8$ as a promising candidate for applications in optoelectronic devices. To construct the self-powered photodetectors, $Nb_2Pd_3Se_8$ is synergistically integrated with 2D-TMDs, forming a type-I band alignment that creates a unilateral depletion region, enabling efficient photocarrier separation and collection at V_{DS} = 0 V. Leveraging the gate-tunable band alignment and the different influences of electrostatic doping to $Nb_2Pd_3Se_8$ and TMDs, we successfully achieve a modulation of built-in potential and photodiode behavior. This results in the reverse of band bending and photocurrent flow direction between the two layers. The gate-controlled negative and positive photocurrents switching with linear power-dependent is utilized to show the pixel in the convolution layer, performing multiple tasks such as edge detection and sharpness for in-sensor image processing. Furthermore, the active region is confined to a 1D vdW interface, resulting in the concentration of light into deep-subwavelength scales. This confinement leads to an enhanced accumulation of hot carriers, facilitating the efficient collection of high-energy photons[44,45] for high device performance. Consequently, the device achieves remarkable responsivity under illumination at 375 nm, a fast response time, high detectivity, and a broad spectral detection range from 375 to 1062 nm.

2. Results and Discussion

The gate-controllable negative and positive photoresponse is essential to emulate positive and negative weights for extracting important features from the input image signal in the in-sensor convolutional processing.[7,15] Consequently, we concentrate on modulating the bipolar photoresponse, and the potential of 1D vdW heterojunction is also revealed in our device. To construct a 1D vdW interface for an individual pixel in the image sensor, the self-powered photodetectors (V_{DS} = 0 V) based on a 1D-$Nb_2Pd_3Se_8$/2D WSe_2 mixed-dimensional heterostructure were fabricated via a dry transfer system-assisted heterostructure staking process, as illustrated in **Figure 1a**. Further details on the device fabrication process and $Nb_2Pd_3Se_8$ synthesis are provided in the Methods section. In a 3 × 3 kernel, all devices share the same drain-source electrodes;[7,8] therefore, self-powered photodetectors (V_{DS} = 0 V) with gate-tunable bipolar photoresponse allow for efficient photocurrent summation, making them well-suited for convolutional in-sensor imaging. The device is equipped with four-terminal electrodes, each serving distinct functions to independently characterize the electronic and optoelectronic properties of $Nb_2Pd_3Se_8$, WSe_2, and the heterostructure. Figures 1b,c present the scanning electron microscope (SEM) and atomic force microscopy (AFM) images of the device with the white scale bar corresponding to 5 µm. The Raman characterization of $Nb_2Pd_3Se_8$ and WSe_2 was examined, as shown in Figure S1 (Supporting Information). Further characterization of $Nb_2Pd_3Se_8$ is presented in Figure S2 (Supporting Information), which includes X-ray diffraction (XRD), SEM image, and AFM analyses, and Figure S3 (Supporting Information), which provides scanning transmission electron microscopy (STEM) images of the $Nb_2Pd_3Se_8$ surface. XRD results confirm the successful synthesis of single-crystal $Nb_2Pd_3Se_8$, while the crystal photograph highlights its needle-like wire structure in bulk form. The SEM and AFM analyses provide quantitative data on the nanowire

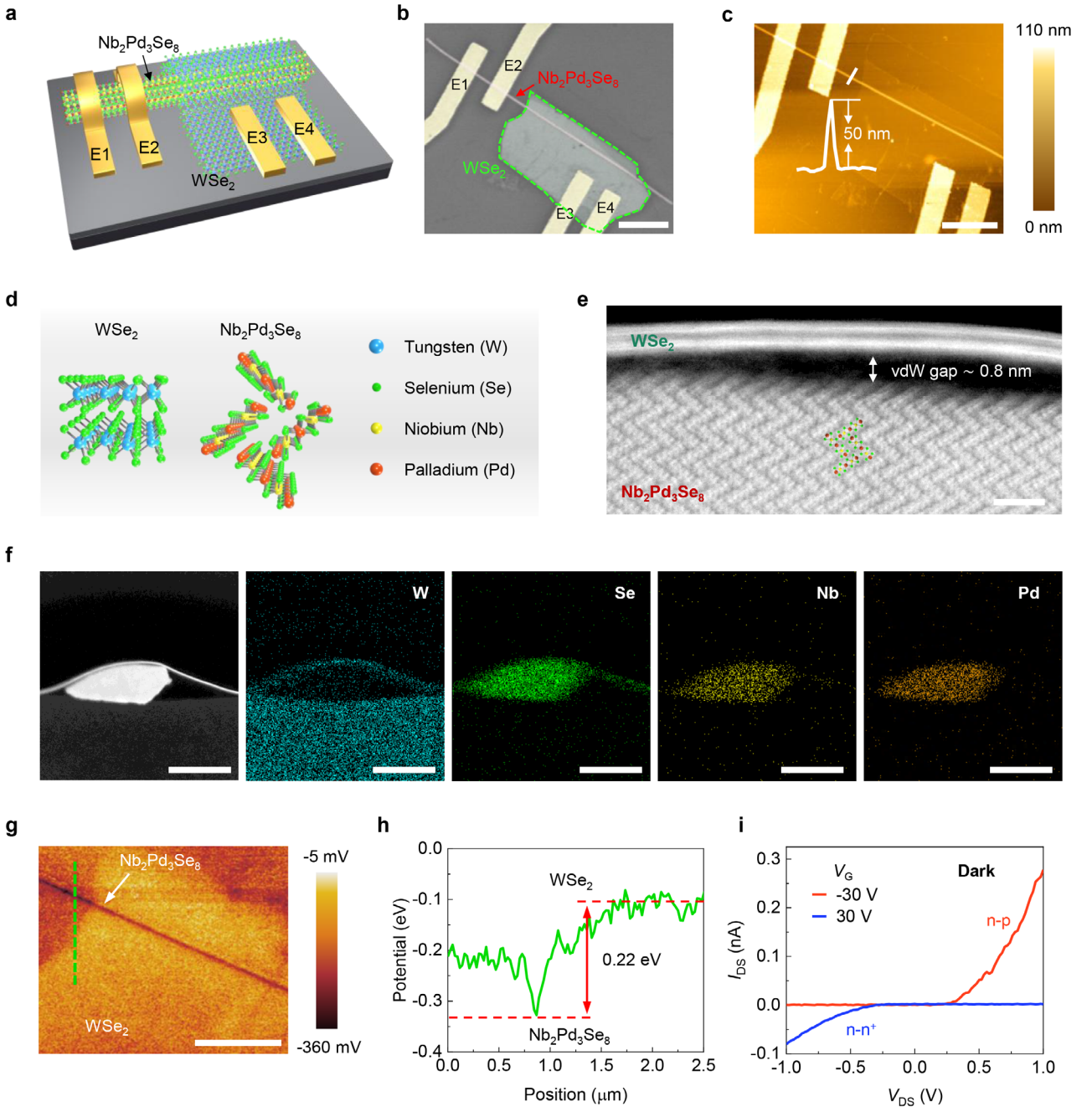

Figure 1. Electrical and material characterizations of 1D $Nb_2Pd_3Se_8$/2D WSe_2 heterostructure photodetectors. a) Schematic of the fabricated $Nb_2Pd_3Se_8$/WSe_2 vdW heterostructure device. b) SEM and c) AFM image of the device with the white scale bar is 5 μm. The white profile inset in the AFM results corresponds to the material thickness. d) The schematic illustration of $Nb_2Pd_3Se_8$ and WSe_2 crystal structures. e) The cross-sectional STEM image of the device reveals a vdW gap of ≈0.8 nm, indicating a clean interface between two materials and the zigzag morphology of the $Nb_2Pd_3Se_8$ nanowire; the scale bar is 2 nm. f) The elemental mapping results via STEM energy dispersive spectroscopy, with the scale bar corresponding to 50 nm. g) The KPFM surface potential image of $Nb_2Pd_3Se_8$/WSe_2 1D heterojunction with the scale bar is 1 μm, and h) the potential profile of the green dashed line from the KPFM image. i) Output characteristics of the $Nb_2Pd_3Se_8$/2D WSe_2 heterostructure photodetectors with $V_G = -30$ V (red curve) and $V_G = 30$ V (blue curve) under dark conditions.

dimensions, including diameter and length. The STEM images illustrate the stacking arrangement of individual 1D nanowires within the bulk material. The mechanical exfoliation process used to obtain nanowires from the bulk material is described in detail in the Methods section. The crystal structure schematic of WSe_2 and $Nb_2Pd_3Se_8$ is described in Figure 1d. A single-layer WSe_2 includes a tungsten (W) atom that is hexagonally encircled by six other W atoms, sandwiched by two hexagonal close-packed planes of selenium (Se) atoms, with the Se atoms adopting trigonal prismatic coordination around the W atom, and each

layer is bonded together by weak van der Waals forces. Bulk $Nb_2Pd_3Se_8$ unit ribbons are connected in a zigzag shape, the unit ribbon with two niobium (Nb)-centered, edge-sharing Se trigonal prisms linked by palladium (Pd) atoms and flanked by additional Pd atoms, where the inter-ribbon bonding through terminal Pd and trans-Se atoms exhibits a weak van der Waals interaction with a binding energy of 0.39 eV per atom.[41,42] Figure 1e shows the cross-sectional STEM image of the $WSe_2/Nb_2Pd_3Se_8$ heterostructure, illustrating the heterojunction formed through van der Waals interactions with an interlayer spacing of ≈0.8 nm. The STEM analysis reveals an atomically clean interface between two layers devoid of detectable residues, gaps, or contaminants. The clean interfacial condition enables efficient charge transfer between each functional layer. Additionally, the homogeneous spatial distribution of each constituent element was confirmed through STEM energy dispersive spectroscopy (EDS) for elemental mapping, as depicted in Figure 1f.

To accurately verify 1D type-I junction formation, we conduct the kelvin probe force microscopy (KPFM) measurement. Figures 1g,h presents the surface potential imaging and the extracted potential line profile of $Nb_2Pd_3Se_8/WSe_2$ heterostructure, respectively. The $Nb_2Pd_3Se_8$ surface potential is ≈0.22 eV lower than that of WSe_2. Based on the results, the narrow bandgap $Nb_2Pd_3Se_8$ and WSe_2 band alignment is provided (Figure S4, Supporting Information). The 1D overlapping heterojunction region exhibits a sharp surface potential gradient, serving as the principal active area for photocurrent generation via the photovoltaic effect. The photoresponse mapping using conductive-AFM (C-AFM) under 375 nm laser illumination, shown in Figure S5 (Supporting Information), confirms that photocurrent generation is primarily localized at the 1D vdW heterojunction. This corresponds to the 1D surface potential gradient observed in the KPFM results, indicating subwavelength confinement of the active region. The transfer characteristics of $Nb_2Pd_3Se_8$, WSe_2, and 1D heterojunctions are revealed as shown in Figure S6 (Supporting Information). $Nb_2Pd_3Se_8$ exhibits n-type semiconductor characteristics, while WSe_2 demonstrates ambipolar behavior with carrier density significantly influenced by the gate voltage (V_G). In all measurements of the $Nb_2Pd_3Se_8/WSe_2$ photodetector conducted in this study, the $Nb_2Pd_3Se_8$ terminal served as the grounded electrode. Figure 1i illustrates the output curve characteristics under applied negative (−30 V) and positive (30 V) V_G for the conducted measurements. As a result of gate-controlled band alignment, the heterojunction can switch from an n-type ($Nb_2Pd_3Se_8$)/p-type (WSe_2) configuration to an n-type ($Nb_2Pd_3Se_8$)/n^+-type (WSe_2) configuration, leading to reverse rectification. As demonstrated in our electrostatic simulation results using COMSOL Multiphysics, we modeled the $Nb_2Pd_3Se_8/WSe_2$ heterostructure under back-gate voltages (Figure S7, Supporting Information). The simulation results demonstrate that the electrostatic potential in the WSe_2 and the heterojunction region is strongly modulated by the gate, while $Nb_2Pd_3Se_8$ connected to ground exhibits much weaker potential variation. As a result, the band bending occurs primarily in the WSe_2 channel and heterojunction, enabling reconfiguration of the heterojunction under varying V_G. Therefore, the gate-tunable built-in electric field (reverse bending) facilitates the photocarrier transfer in the opposite direction.

2.1. High-Performance $Nb_2Pd_3Se_8$ Photodetector

Despite its potential for a 1D integrated optoelectronic device,[41] there is a lack of reports on the electrical properties of $Nb_2Pd_3Se_8$ at temperatures below 77K and the response speed of $Nb_2Pd_3Se_8$ photodetectors. Therefore, we first present the study detailing the performance of the $Nb_2Pd_3Se_8$ photodetector and its temperature-dependent electrical characteristics to provide the potential of $Nb_2Pd_3Se_8$ for advanced optoelectronic device applications. **Figure 2a** displays the transfer characteristics of the $Nb_2Pd_3Se_8$ field-effect transistor (FET) with temperature dependence ranging from 30 to 300 K. As the temperature decreases, there is a gradual reduction in the current level, indicative of semiconductor-like transport behavior. The $Nb_2Pd_3Se_8$ exhibits n-type behavior across various temperatures, with a decline in temperature leading to a decrease in "off"-current levels due to the diminished thermionic injection and suppressed trap-assisted transport.[46] The photocurrent response of the $Nb_2Pd_3Se_8$-based photodetector under various laser exposures is depicted in Figure 2b. The photocurrent I_{ph} is determined as $I_{ph} = I_{light} - I_{dark}$, where I_{light} and I_{dark} denote the drain-source current (I_{DS}) with and without light illumination, respectively. The $Nb_2Pd_3Se_8$ photodetector exhibits a wide range of photodetection (375–1062 nm) due to its narrow bandgap. When $V_{DS} = 1$ V, the release of photocarriers under 375 nm laser illumination exhibits a slower response than that observed in other lasers due to the photogating effect being dependent on the wavelength of the laser.[47]

The photocurrent and the responsivity with power density dependence under applied $V_{DS} = 1$ V and 642 nm laser wavelength illumination are demonstrated as shown in Figure 2c,d. The photocurrent and power density (P) relationship can be well-fitted using the formula $I_{ph} \approx P^{\alpha}$. An α value of 0.88 is obtained, with $\alpha < 1$ implying that the device is influenced by the photogating effect, in which the photo-induced charging and trapping contribute to the recombination processes.[47] The responsivity is obtained by the formula $R = I_{ph}/PS$ where P denotes the light power density and S is the active area.[48] The responsivity of the $Nb_2Pd_3Se_8$ photodetector under 640 nm laser illumination is up to 5.3 A W^{-1}, corresponding to an incident laser power of 0.3 nW μm^{-2}. To explore the trap-induced trade-off between responsivity and response speed, we demonstrate the fast photocurrent response measurement as shown in Figure 2e. The $Nb_2Pd_3Se_8$-based photodetector achieves a high responsivity whereas ensuring a fast response speed of 68.8 µs, indicating that $Nb_2Pd_3Se_8$ is desirable for a broadband photodetector with high performance and fast response time. $Nb_2Pd_3Se_8$-based photodetector demonstrates significant potential for miniaturizing optoelectronic devices. Nevertheless, the photovoltaic effect, which enables the switching of negative and positive photocurrent, is not observed in photodetectors that are solely composed of $Nb_2Pd_3Se_8$ nanowires.

2.2. Gate-Tunable Broadband Bi-Directional Photoresponse

Our study substantiates the consistent bi-directional photoresponse in $Nb_2Pd_3Se_8/WSe_2$ self-powered photodetector ($V_{DS} = 0$ V) by fabricating an additional device with different WSe_2 and $Nb_2Pd_3Se_8$ thicknesses and higher performance. The

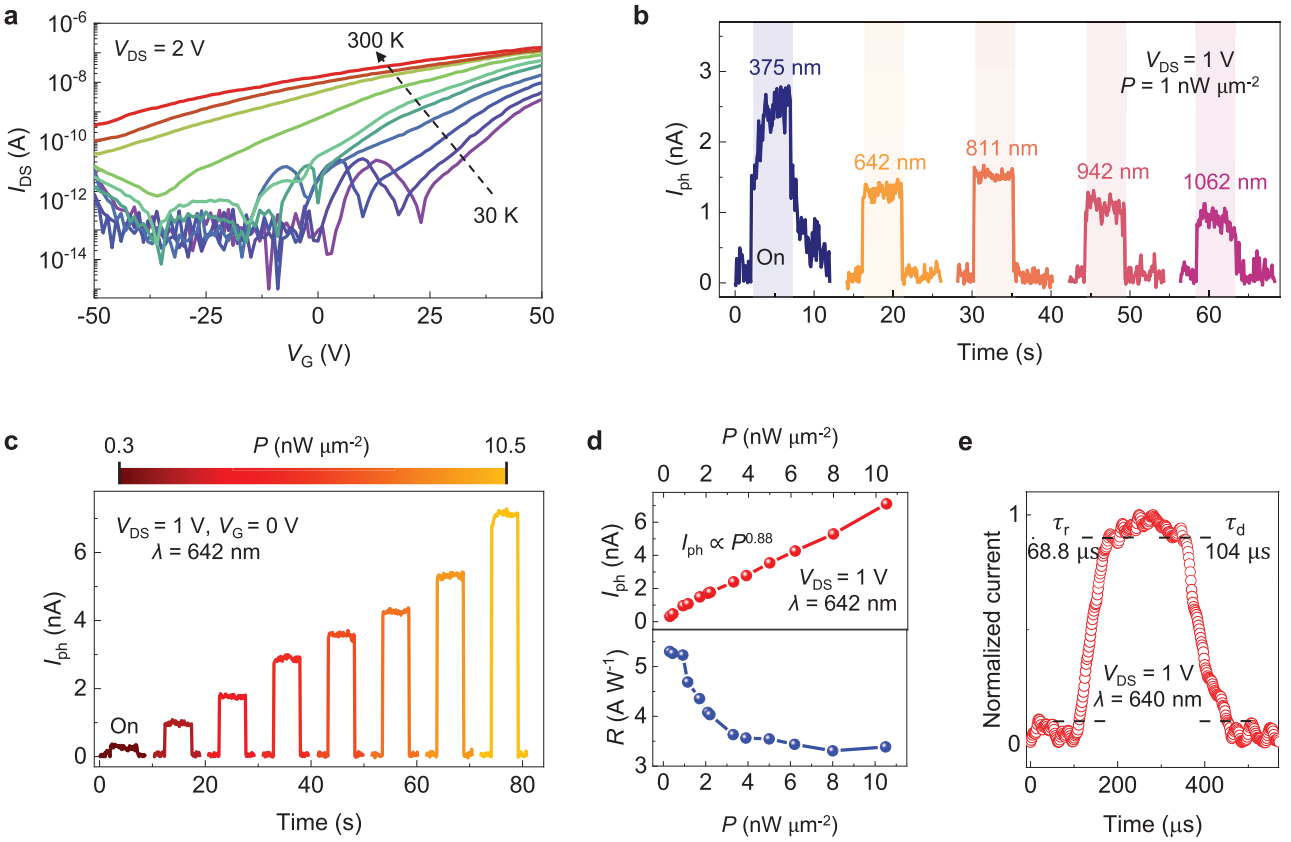

Figure 2. Electrical and photoresponse properties of the $Nb_2Pd_3Se_8$ phototransistor. a) Transfer curves with temperature-dependent ranging from 30 to 300 K at V_{DS} of 2 V plotted in a logarithmic scale. b) The photoresponse as a function of time at different laser wavelengths illumination under applied V_{DS} = 1 V and P = 1 nW μm^{-2}. c) The time-dependent photocurrent of the photodetector under 642 nm laser wavelength illumination with different power intensities at V_{DS} = 1 V. d) The top is the power dependence of the measured photocurrent at V_{DS} = 1 V and 642 nm illumination with an exponential fitting between photocurrent and power densities. The bottom is the calculated R with power dependence. e) Fast time-resolved photocurrent response at V_{DS} = 1 V and λ = 642 nm, which is read out by an oscilloscope. The rise time τ_r = 68.8 μs and decay times τ_d = 104 μs.

bipolar photoresponse capability of the device shown in Figure 1 is demonstrated in Figure S8 (Supporting Information). The optical image of the new device is shown in **Figure 3a**, where the red line indicates the 1D $Nb_2Pd_3Se_8$, and WSe_2 is denoted by the green contour part. The scale bar corresponds to 10 μm. The corresponding AFM and KPFM results are detailed in Figure S9 (Supporting Information), where they demonstrate that the work function of $Nb_2Pd_3Se_8$ remains lower than that of WSe_2, thereby maintaining the formation of a type-I junction and unilateral depletion region.[19,43] Figures 3b,c exhibit the photocurrent response under varying laser wavelengths (375, 642, 811, 942, and 1062 nm) at V_G = −20 and 0 V, respectively, for the newly constructed device. The results illustrate stable and reproducible broadband photocurrent modulation. The negative and positive photocurrents are exhibited under varying applied V_G (V_G = −20 V for negative photocurrent and V_G = 0 V for positive photocurrent). The gate-tunable reverse diode rectification switching, as well as the transfer characteristics, are shown in Figures S10,S11 (Supporting Information), indicating the gate-tunable reverse rectification behavior under dark current. The photocurrent induced by the photovoltaic effect results in a minimal dark current of ≈4.8 × 10^{-15} A at V_G = −20 V and 5.2 × 10^{-15} A at V_G = 0 V (Figure S9, Supporting Information), facilitating distinct on-off behavior and an on-off current ratio above 10^3 under illumination at 375 nm (photon energy ≈ 3.3 eV). To further evaluate the device performance, we directly measured the noise spectral density of the $Nb_2Pd_3Se_8/WSe_2$ heterostructure photodetector under dark conditions at room temperature and zero bias (V_{DS} = 0 V). The measured noise spectrum is presented in Figure S12 (Supporting Information), from which the specific detectivity (D^*) was calculated using the standard expression: $D^* = (R\sqrt{A})/(\sqrt{NPSD})$, where $NPSD \approx 4 \times 10^{-32}$ A^2 Hz^{-1} (measured noise power spectral density). The calculated detectivity is ≈6.35 × 10^{10} Jones confirms the operational capability and functionality of the device.

Corresponding to photocurrent values, the calculated responsivity with laser wavelength dependence at V_G = −20 and 0 V is shown in Figures 3d,e, respectively. The predominant photocurrent generation occurs at the overlapped heterojunction, as depicted in Figure S13 (Supporting Information), the photocurrent mapping. In our devices, the photocurrent generation mechanism originates primarily from the photovoltaic effect. The contributions from the Giant bulk piezophotovoltaic effect and asymmetric Schottky contacts[15,49] cannot be avoided.

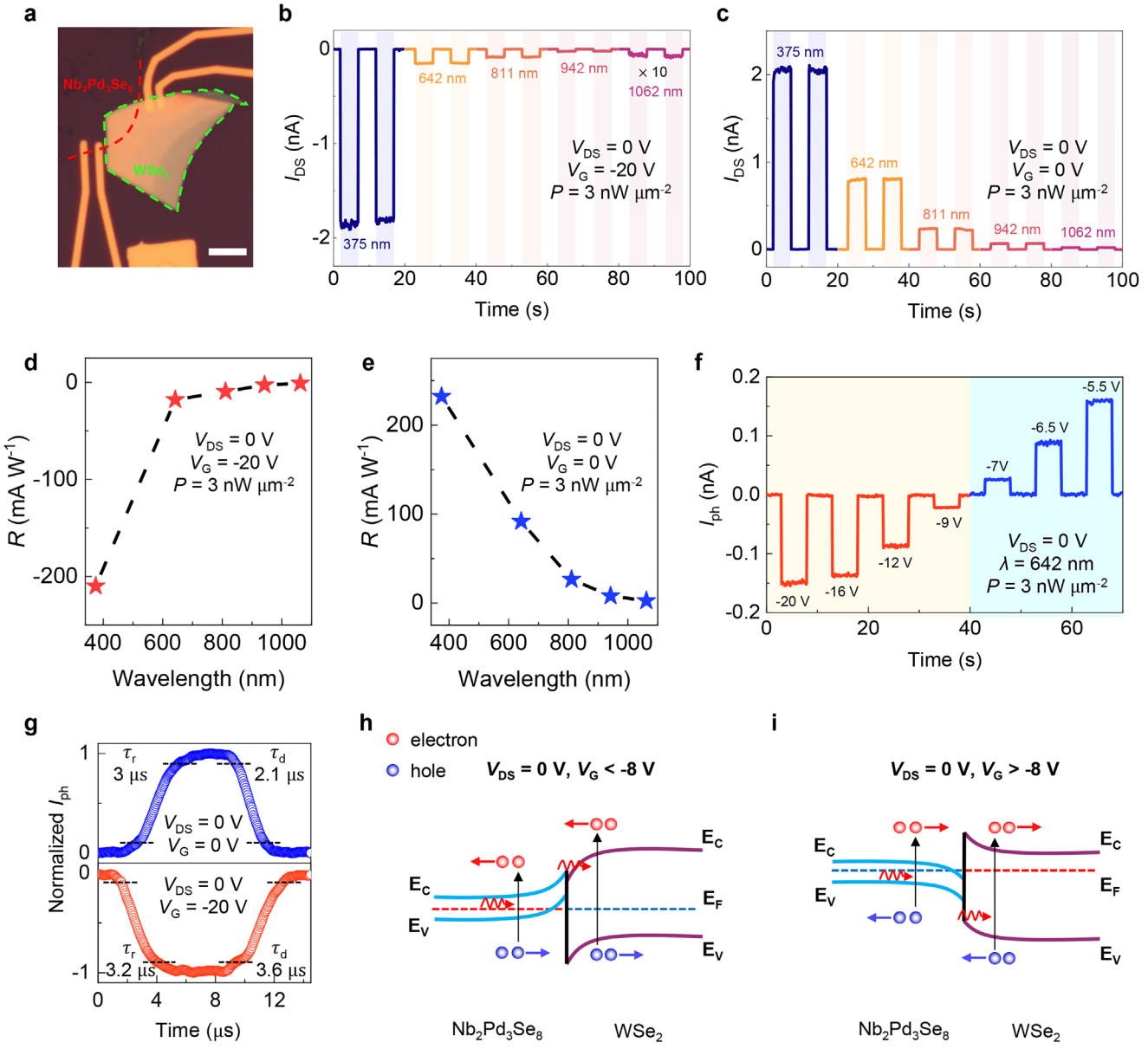

Figure 3. Gate-controlled broadband negative and positive photocurrent response of a new $Nb_2Pd_3Se_8$/ WSe_2 heterostructure photodetector. a) The optical image of the new $Nb_2Pd_3Se_8$/ WSe_2 device, with the scale bar corresponding to 10 μm. b,c) Negative and positive photoresponse under different laser wavelengths (375, 642, 811, 942, and 1062 nm) illumination at V_{DS} = 0 V and P = 3 nW μm^{-2} with applied V_G = −20 and 0 V, respectively. d,e) The calculated R with different lasers at fixed P = 3 nW μm^{-2} corresponds to V_G = −20 and 0 V, respectively. f) Gate-tunable negative and positive photocurrent switching under illumination at 642 nm with P = 3 nW μm^{-2}. g) The rise and decay times for negative (V_G = −20 V) and positive (V_G = 0 V) photovoltaic effects. h,i) The schematic of $Nb_2Pd_3Se_8$/ WSe_2 band alignments at different V_G < −8 V h) and V_G > −8 V i) for negative and positive photoresponse, respectively. The red arrows correspond to the movement direction of electrons, while the blue arrows are the direction of holes.

However, their signals and influences on the overall photocurrent generation are significantly lower in comparison to the photovoltaic effect of heterojunction.[15,49] The active area is therefore defined as the 1D overlapped heterojunction region of the device for responsivity calculation,[28,29] with the estimated active area being ≈3 μm.^{2} The 1D active area enables light confinement at deep-subwavelength scales, enhancing hot carrier accumulation and facilitating efficient high-energy photon collection. Consequently, the device achieves high responsivity of up to 232 mA W^{-1} and external quantum efficiency (EQE) of 77% (Figure S14, Supporting Information) under 375 nm laser wavelength illumination. Furthermore, the results reveal a gate-tunable spectral response, attributable to variations in the absorption spectra of the constituent flakes and the gate-induced modulation of band alignment.[50,51] Exploiting this characteristic may broaden the device application to miniaturized spectrometers.[50–53] Figure 3f illustrates the gate-manipulable transition between negative and positive photocurrent under a

power density of $P = 3$ nW μm^{-2} at 642 nm, with the switching point estimated to be $V_G = -8$ V. The gate bias value is determined by the original band alignment between $Nb_2Pd_3Se_8$ and WSe_2 at $V_G = 0$ V. At $V_G = -8$ V, the band bending approaches a nearly flat configuration, resulting in a minimal photocurrent generation. Variations above and below this V_G value trigger an inversion in band bending, thereby reversing the direction of photocarrier transport. The response times for both negative and positive photocurrents at a wavelength of 642 nm are depicted in Figure 3g. With photocurrent generation driven by the photovoltaic effect at $V_{DS} = 0$ V, we achieve rapid response and decay times for both negative and positive photocurrents, making the device highly suitable for high-speed broadband image sensors. Additionally, persistent photoconductivity remains negligible, even under 375 nm laser illumination, as shown in Figures 3b,c.

To elucidate the operational principles of the device, we illustrate the band alignment for negative and positive photocurrent generation mechanisms in Figure 3i, respectively. The V_G induces the modulation of the Fermi levels in $Nb_2Pd_3Se_8$ and WSe_2, effectively manipulating the built-in electric field and thereby directing the drift current under light illumination. Under applied $V_G < -8$ V, the band bending toward $Nb_2Pd_3Se_8$, the configuration of an n-type $Nb_2Pd_3Se_8$ and p-type (or n−type) WSe_2 heterostructure is formed. Consequently, electrons move toward $Nb_2Pd_3Se_8$, and the holes transfer in an opposite direction under light illumination (negative photocurrent in Figure 3b). For $V_G > -8$ V, WSe_2 becomes more n-type behavior, this reconfigures the heterostructure gradually to be n-type $Nb_2Pd_3Se_8$ and n^+-type WSe_2 heterojunction, leading to the band bending toward WSe_2. As a result, electrons migrate toward WSe_2, and direct holes transport oppositely under light illumination (positive photocurrent in Figure 3c). Additionally, depending on the wavelength of laser excitation, electron-hole pairs may acquire sufficient energy to overcome the potential barrier, resulting in an enhanced photocurrent signal[50] (the high photocurrent response at a laser wavelength of 375 nm at both $V_G = -20$ and 0 V in Figures 3b,c). The efficient collection of high-energy photons (3.3 eV) is facilitated by the confinement of the charge carriers within a 1D active area. Photocarriers are concentrated into deep-subwavelength volumes, thereby enhancing the possibility of achieving a higher concentration of hot carriers.[44] Additionally, the narrow bandgap $Nb_2Pd_3Se_8$ not only serves as an absorption layer but also acts as a carrier-selective layer within a unilateral depletion region, resulting in high-performance photovoltaic devices.[19]

2.3. Linear Power-Dependent Photovoltaic Response

The laser power-dependent measurement of $Nb_2Pd_3Se_8/WSe_2$ 1D heterojunction was investigated to further elucidate its photovoltaic characteristics. **Figure** 4a,b illustrate the I_{DS}-V_{DS} curves at $V_G = -20$ and 0 V, respectively, with varying light power density under 375 nm laser wavelength illumination. As the light power intensifies, the short-circuit current (I_{SC}) correspondingly escalates, demonstrating both negative and positive I_{SC} modulations in alignment with the observed positive and negative photocurrent responses in Figure 3b,c. Under illumination at an intensity of 3.9 nW μm^{-2}, an I_{SC} of −2.6 nA and an open-circuit voltage (V_{OC}) of 0.3 V are obtained at a gate V_G of −20 V. Similarly, at $V_G = 0$ V, the device exhibited an $I_{SC} = -2.67$ nA and a $V_{OC} = -0.41$ V. The correlation between photocurrent and power density for both V_G is illustrated through fitted curves using the formula $I_{ph} \approx P^{\alpha}$ as shown in Figure 4c. The extracted α is close to 1, confirming the linear relationship of I_{ph} and incident P.

Figures 4d,e show the power-dependent output characteristics of the device under illumination at 642 nm when $V_G = -20$ V (d) and 0 V (e) were applied. At $V_G = 0$ V, a large V_{OC} of up to 0.63 V is achieved under $P = 15$ nW μm^{-2}. The V_{OC} at $V_G = -20$ V is notably lower than at $V_G = 0$ V, this outcome differs markedly from the results under 375 nm illumination. This variation is attributed to the lower photon energy of 642 nm (≈1.94 eV) laser wavelengths, where photocarriers lack sufficient energy to overcome the barrier. Additionally, at $V_G = 0$ V, a unilateral depletion region is established, leading to a high V_{OC}.[19] However, at $V_G = -20$ V, gate-tunable band alignment induces the gradual formation of a type-II heterojunction at the $Nb_2Pd_3Se_8$ and WSe_2 interface, resulting in a decrease in both V_{OC} and I_{SC} as well. The power-dependent output characteristics at an 811 nm laser wavelength are presented in Figure S13 (Supporting Information), demonstrating a high V_{OC} at $V_G = 0$ V and a significantly lower V_{OC} at $V_G = -20$ V, mirroring the trends observed under 642 nm illumination. Notably, at $V_G = -20$ V, the device exhibits a significantly higher V_{OC} and I_{SC} under 375 nm illumination in comparison to the performance at 642 and 811 nm laser wavelengths. These findings suggest that our device architecture is conducive to efficient high-energy photon collection.[44] The linearity of I_{ph} on P is confirmed for 642 nm laser wavelengths, as shown in Figure 4f, the photocurrent with power dependence. The photocurrent exhibits a linear increase with P in which $\alpha \approx 1$. Additionally, within the defined variations of wavelengths and gate bias (V_G can range from −20 to 0 V), the photocurrent displays a linear dependency on illumination intensity. The linear dependence on P is essential for convolutional processing, facilitating accurate analog multiplication between P and a programmed value of R.[13]

We display the gate-dependent photoresponsivity for different laser wavelengths 642, 375, and 811 nm as shown in Figure 4g–i, respectively, to denote the programming voltage (Vp). The difference in the influences of laser wavelengths on negative and positive weight is attributable to the distinct absorption spectra of $Nb_2Pd_3Se_8$ and WSe_2 coupled with variations in photon energy (Figures 3h,i the mechanism schematic). These factors are instrumental in modulating the modulation of I_{sc} and the open-circuit voltage (V_{oc}) (Figures 4a–f; S15, Supporting Information). Additionally, the reproducibility of gate-tunable bipolar photoresponse in $MoSe_2$ and MoS_2 is also demonstrated in Figures S16–S20 (Supporting Information). Need to note that $Nb_2Pd_3Se_8$ exhibits a well-suited band alignment with various TMDs, particularly $MoSe_2$ (Figure S20, Supporting Information), enabling negative and positive photocurrent switching. The $Nb_2Pd_3Se_8$ /$MoSe_2$ heterostructure demonstrates an optimal balance of negative and positive photocurrents, with a switching gate voltage close to 0 V, making it desirable for high-performance in-sensor imaging.

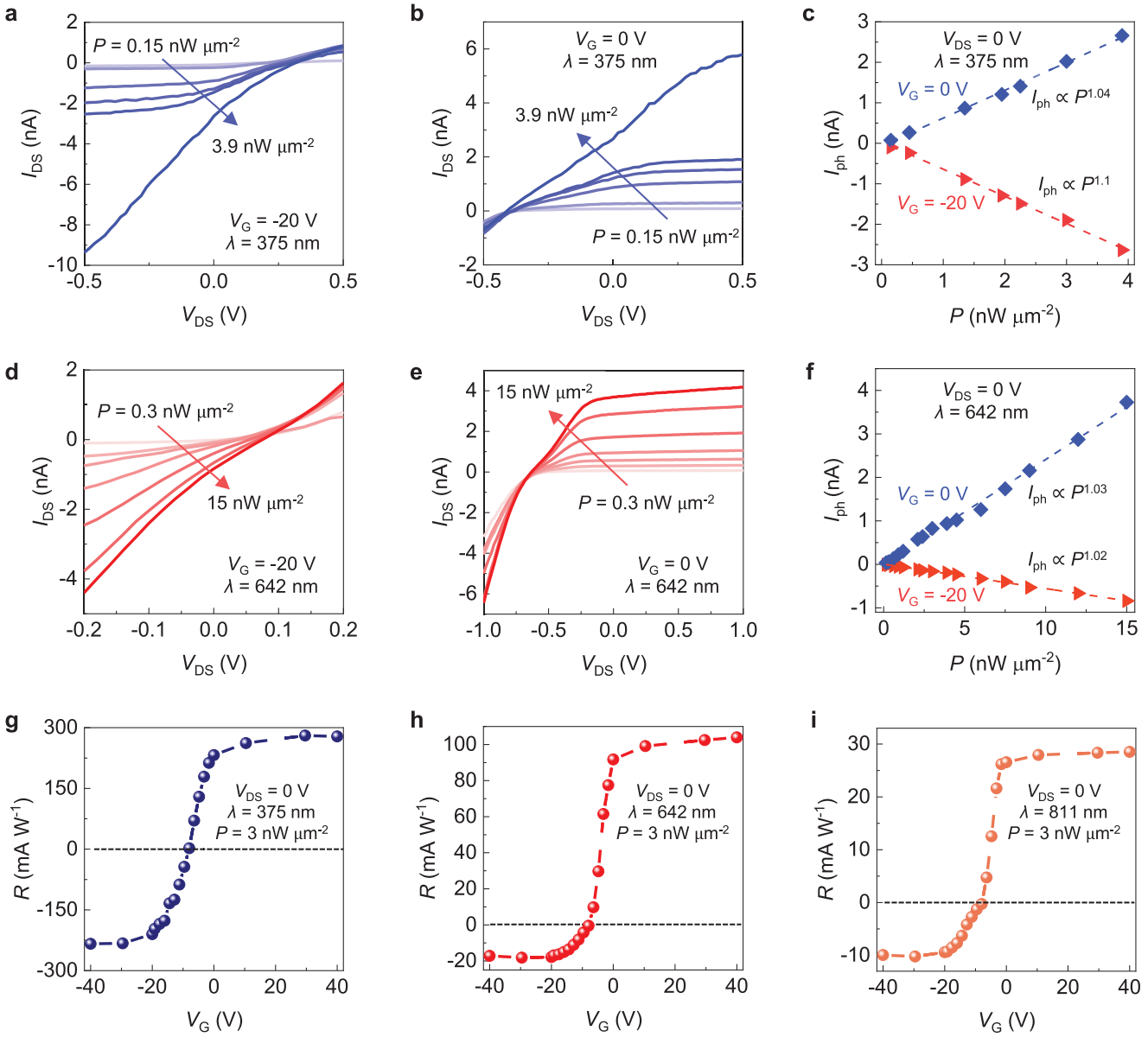

Figure 4. Photovoltaic response of $Nb_2Pd_3Se_8$/ WSe_2 1D vdW photodetector. a,b) The output curve of $Nb_2Pd_3Se_8$/ WSe_2 photodetector with different power densities under illumination at 375 nm, a) $V_G = -20$ V, b) $V_G = 0$ V. c) The dependence of the extracted I_{ph} from I_{SC} for different gate voltages under 375 nm laser wavelength illumination with linear fitting curve. d,e) The power-dependent output characteristics of the devices under 642 nm illumination with applied $V_G = -20$ and 0 V, respectively. f) I_{ph} with power-dependent under illumination at 642 nm. Linear power dependence is crucial for accurately depicting pixel grayscale levels through variations in light power densities. g–i) The calculated R for g) 375 nm, (h) 642 nm, ma which is used for convolutional kernel demonstration, and i) 811 nm laser wavelengths with V_G in the range from −40 to 40 V.

2.4. In-Sensor Image Processing with 1D vdW Heterostructure

Figure 5a schematically depicts the operational mechanism of in-sensor image processing utilizing a gate-tunable photovoltaic heterostructure photodetector. For demonstration purposes, a top 3 × 3 matrix corresponding to optical input and a central 3 × 3 filter kernel are programmed to extract features from the object for processing purposes. The individual pixel device in the convolutional kernel is fabricated by utilizing the gate-tunable negative and positive photoresponse in a 1D-$Nb_2Pd_3Se_8$/2D-WSe_2 self-powered photodetector ($V_{DS} = 0$ V). For optimal photocarrier collection and accurate estimation of the effective light absorption area, it is recommended that the contact electrodes of the heterojunction device penetrate through the material and be positioned as close as possible to the 1D vdW junction. The input signals related to the incident laser power P_{in}, where $P_{in} = P \times A$. The output photocurrent is achieved by $I_j = \sum R_{ij} \times P_{ij}$ where the total current is derived by a cross-bar array (Figure S21, Supporting Information), leveraging Kirchhoff's law for its computation.[3,8] The targeted output can be achieved by electrostatically modulating photoresponsivity, where specific photoresponsivity values correspond to negative and positive values required for the

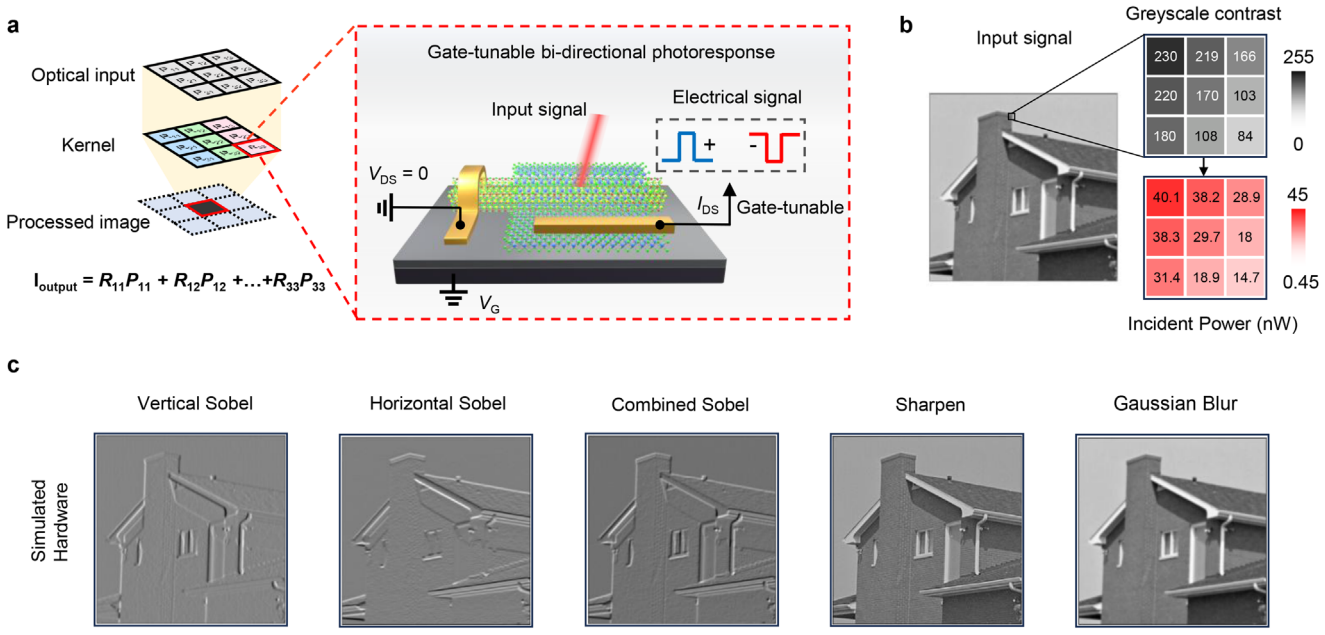

Figure 5. The simulation of $Nb_2Pd_3Se_8$/ WSe_2 1D vdW heterostructure for in-sensor image processing. a) Schematic of in-sensor image processing with the kernel pixels utilizes the gate-tunable negative and positive photocurrent switching in $Nb_2Pd_3Se_8$/ WSe_2 heterostructure device. The incident illumination serves as the input signals while photocurrent output is gate-tunable negative and positive weights. As a result, the *R* of each kernel can be dynamically modulated via V_G, facilitating the adaptation to diverse filter kernel functionalities. b) The 8-bit grayscale original image is derived from the analog conversion of laser intensity, with the inset 3 × 3 patch demonstrating the correlation between grayscale contrast and the resultant incident power. c) Simulation of the hardware for different image processing results using achieved *R* results (including vertical Sobel, horizontal Sobel, combined Sobel, sharpen, and Gaussian blur) with in-sensor computing (top) and simulation (bottom).

implementation of in-sensor optoelectronic computing. By applying the local V_G to each 1D vdW heterostructure device, it is feasible to obtain both negative and positive values of R_{ij}. This approach enables the creation of a reconfigurable in-sensor system capable of simultaneously capturing and processing image data. Consequently, the weights essential for the convolutional process are encoded within the matrix of gate voltages.

To validate this concept, we demonstrate the in-sensor image processing simulation using the achieved results from a 642 nm laser wavelength (visible light). We have used a single device's result to perform each pixel within a 3 × 3 kernel for the simulation process. Utilizing the linearity of power-dependent, the contrast of each image pixel, set to 255 out of 255, is converted to the corresponding input signal P_{in} with power ranging from 0.45 to 45 nW. Figure 5b displays the grayscale representation of the original image, featuring a resolution of 256 × 256 pixels with an 8-bit depth, sourced from the USC-SIPI image database.[54] The inset 3 × 3 top patch shows the greyscale contrast linearly reflects the corresponding optical input signals of P_{in} (bottom). Figure 5c shows the in-sensor processing results using the achieved *R* in our device (Figure 4h) for pixel manipulation within the kernels. This simulation includes various filter kernels, including vertical Sobel, horizontal Sobel, a combination of both vertical and horizontal Sobel, image sharpening, and Gaussian blurring filters. The application of the 3 × 3 matrix of V_G is designed to obtain the appropriate 3 × 3 responsivity matrices, and the simulation results using the standard kernels are depicted in Figure S22 (Supporting Information). The simulated hardware result vividly demonstrates edge feature extraction, image sharpening, and image blurring, closely matching the simulation using the standard kernels. These findings reveal the effectiveness of our 1D vdW heterostructure photosensor for in-sensor image processing.

3. Conclusion

We have demonstrated the gate-tunable broadband bipolar photoresponse in 1D vdW heterojunction via utilizing the novel 1D $Nb_2Pd_3Se_8$/2D TMDs heterostructure for in-sensor image processing. The 1D $Nb_2Pd_3Se_8$ has been successfully synthesized, showing its application in a photodetector with impressive performance: a high *R* up to 5.3 A W^{-1}, a fast response speed of 68.8 µs, and a detectivity of 6.35 × 10^{10} Jones. This highlights the potential of our $Nb_2Pd_3Se_8$ for advanced optoelectronic device applications. Additionally, $Nb_2Pd_3Se_8$ exhibits impressive optical properties, a suitable Fermi energy, and optimal band alignment with various 2D-TMDs (WSe_2, $MoSe_2$, and MoS_2), enabling gate-tunable negative and positive photocurrent switching in 1D/2D heterostructures. The self-powered photodetector has been achieved by integrating $Nb_2Pd_3Se_8$ with 2D-TMDs, establishing a type-I junction and a unilateral depletion region. The active area has been confined to a 1D scale, concurrently addressing the high performance, including fast response speed and broadband photodetection (UV to NIR). The 1D active area enables deep-subwavelength light confinement, enhancing hot carrier accumulation and facilitating the efficient collection of high-energy photons, thereby increasing the sensitivity under 375 nm laser illumination. The tuning of band alignment controlled by the gate voltage results in the modulation between n-p and n-n^+

heterojunction configurations. This strategic adjustment enables us to precisely tune the direction of the generated photocurrent, facilitating the transition between negative and positive photocurrent weight for in-sensor image processing demonstration. Our study also reveals the gate-tunable spectral response facilitated by adjustable band alignment in our 1D vdW heterojunction. The results demonstrate the versatility of our 1D vdW architecture for a wide range of applications, including machine vision, miniaturized spectrometers, and artificial intelligence.

4. Experimental Section

Synthesis of Bulk $Nb_2Pd_3Se_8$ Crystal: First, single crystals of $Nb_2Pd_3Se_8$ were synthesized via the CVT method, and iodine was used as a transport agent. A stoichiometric blend of Nb, Pd, and Se powders underwent heat treatment within the temperature range of 500–700 °C to attain a pure phase of $Nb_2Pd_3Se_8$ powder, serving as a precursor for the subsequent CVT reaction. Then, $Nb_2Pd_3Se_8$ powder was loaded into a 12 cm-long quartz ampoule alongside iodine and subjected to heating at 700 °C for 7 days within a horizontal tube furnace. Post-reaction, elongated needle-like crystals were deposited on the cold end of the quartz ampoule, where a temperature gradient of 80 °C was established.[41]

Mechanical Exfoliation of $Nb_2Pd_3Se_8$: The $Nb_2Pd_3Se_8$ crystal was placed on wafer dicing tape (BT150E-KL, Nitto) and laminated 5–6 times to facilitate exfoliation. A SiO_2/Si substrate was cleaned by ultrasonication in acetone for 3 min, followed by drying at 110 °C for 10 min to remove residual moisture. The polymer tape was then firmly adhered to the substrate using a finger for a few seconds to ensure uniform contact. After that, the tape was slowly peeled off, transferring $Nb_2Pd_3Se_8$ nanowires onto the substrate. The AFM analysis confirmed that most structures maintain a linear morphology (Figure S2, Supporting Information).

Device Fabrication: The obtained $Nb_2Pd_3Se_8$ bulks were mechanically exfoliated on 300 nm thick SiO_2/Si substrates. The few-layer TMDs (WSe_2, $MoSe_2$, MoS_2) (2D Semiconductors) were exfoliated onto the polydimethylsiloxane and then transferred onto the $Nb_2Pd_3Se_8$ flakes via the dry transfer system under an optical microscope-assisted alignment. Finally, the designated electrical electrodes were patterned using electron-beam lithography, and Cr/Au (5/100 nm) metal contacts were deposited via thermal deposition.

Characterization of the Sample (XRD, AFM, KPFM, STEM, Electrical Measurement, Photocurrent Measurement, And Noise Spectral Measurement): X-ray diffraction (XRD, D8 Advance, Bruker) was performed using Cu K_α radiation ($\lambda = 0.154$ nm) at a scanning rate of 5 ° min^{-1}. The Raman spectra were conducted using a commercial NT-MDT instrument equipped with a 532 nm laser. AFM, C-AFM, and KPFM topographical imaging were performed with a Park Systems NX 10. The SEM result was acquired using a JEOL JSM-6510. Cross-section STEM imaging and EDS mappings were achieved with a JEM-ARM300CF from JEOL, Japan. The electrical characteristics and the photocurrent measurement of the fabricated devices were evaluated employing an SMU Keysight/B1500A system alongside laser sources at wavelengths of 375, 642, 811, 942, and 1062 nm provided by RGB Lambda, featuring a beam diameter of ≈1 mm. The photocurrent and electrical measurements were performed under ambient conditions. Measurements of power density were undertaken with a PD300-BB silicon detector coupled to a Nova II Power Meter, using a 20 µm pinhole. The temperature-dependent transfer characteristics of the $Nb_2Pd_3Se_8$ FET were investigated using a Lakeshore cryogenic probe station, with signal detection facilitated by a Keithley 4200-SCS parameter analyzer. The response time of the device was determined using an SR570 pre-amplifier, with data capture conducted via a DSO-X 2002A oscilloscope from Agilent Technologies. Noise current was measured using a DC voltage source, a low-noise current preamplifier (SR570, Stanford Research Systems) to amplify the current signal, and a data acquisition system (NI DAQ-4431) to digitize and record the data (see Figure S23, Supporting Information).

Supporting Information

Supporting Information is available from the Wiley Online Library or from the author.

Acknowledgements

This work was supported by the National Research Foundation of Korea (NRF) grant funded by the Korea government(MSIT) (RS-2024-00356964 and RS-2024-00406152), and by BrainLink program funded by the Ministry of Science and ICT through the National Research Foundation of Korea(RS-2023-00236798).

Conflict of Interest

The authors declare no conflict of interest.

Author Contributions

V.K.D., M.C.N., and B.J.J. contributed equally to this work. V.K.D. and J.-H.K. conceived the idea; V.K.D. and M.C.N. conducted device fabrication; V.K.D., M.C.N., N.T.D., C.H., and W.J.Y. performed device performance measurements; N.T.D. and V.K.D. conducted the in-sensor image processing; B.J.J., J.K., X.Z., and J.-Y.C. prepared the CVT $Nb_2Pd_3Se_8$ samples; D.H.P. and V.D.D. handled electrode patterning and metal deposition; V.T.V. performed the Raman measurements; V.K.D., M.C.N., and J.-H.K. analyzed the data, interpreted the results, and wrote the original manuscript; M.C.N., V.K.D., V.D.D., W.J.Y., R.A.T, K.K., and J.-H.K. contributed to the review and editing of the manuscript. All authors participated in discussions on the results and manuscript preparation. J.-H.K. supervised the project.

Data Availability Statement

The data that support the findings of this study are available from the corresponding author upon reasonable request.

Keywords

1D vdW heterostructure, broadband photodetection, convolution image processing, gate-tunable bi-directional photoresponse, vdW heterostructure-based in-sensor computing

Received: January 1, 2025
Revised: July 25, 2025
Published online:

[1] F. Zhou, Y. Chai, *Nat. Electron.* **2020**, *3*, 664.
[2] L. Mennel, J. Symonowicz, S. Wachter, D. K. Polyushkin, A. J. Molina-Mendoza, T. Mueller, *Nature* **2020**, *579*, 62.
[3] T. Wan, B. Shao, S. Ma, Y. Zhou, Q. Li, Y. Chai, *Adv. Mater.* **2023**, *35*, 2203830.
[4] Y. Li, S. Chen, Z. Yu, S. Li, Y. Xiong, M. E. Pam, Y. W. Zhang, K. W. Ang, *Adv. Mater.* **2022**, *34*, 2201488.
[5] N. T. Duong, Y.-C. Chien, H. Xiang, S. Li, H. Zheng, Y. Shi, K.-W. Ang, *Adv. Intelligent Syst.* **2023**, *5*, 2300009.
[6] D. Lee, M. Park, Y. Baek, B. Bae, J. Heo, K. Lee, *Nat. Commun.* **2022**, *13*, 5223.
[7] G. Wu, X. Zhang, G. Feng, J. Wang, K. Zhou, J. Zeng, D. Dong, F. Zhu, C. Yang, X. Zhao, D. Gong, M. Zhang, B. Tian, C. Duan, Q. Liu, J. Wang, J. Chu, M. Liu, *Nat. Mater.* **2023**, *22*, 1499.

[8] N. T. Duong, Y. Shi, S. Li, Y. C. Chien, H. Xiang, H. Zheng, P. Li, L. Li, Y. Wu, K. W. Ang, *Adv. Sci.* **2024**, *11*, 2303447.
[9] G. Cao, P. Meng, J. Chen, H. Liu, R. Bian, C. Zhu, F. Liu, Z. Liu, *Adv. Funct. Mater.* **2020**, *31*, 2005443.
[10] M. Xu, X. Chen, Y. Guo, Y. Wang, D. Qiu, X. Du, Y. Cui, X. Wang, J. Xiong, *Adv. Mater.* **2023**, *35*, 2301063.
[11] D. Jayachandran, A. Pannone, M. Das, T. F. Schranghamer, D. Sen, S. Das, *ACS Nano* **2023, 17, 168**.
[12] S. Hong, H. Cho, B. H. Kang, K. Park, D. Akinwande, H. J. Kim, S. Kim, *ACS Nano* **2021**, *15*, 15362.
[13] H. Jang, H. Hinton, W.-B. Jung, M.-H. Lee, C. Kim, M. Park, S.-K. Lee, S. Park, D. Ham, *Nat. Electron.* **2022**, *5*, 519.
[14] P. Yao, H. Wu, B. Gao, J. Tang, Q. Zhang, W. Zhang, J. J. Yang, H. Qian, *Nature* **2020**, *577*, 641.
[15] L. Pi, P. Wang, S.-J. Liang, P. Luo, H. Wang, D. Li, Z. Li, P. Chen, X. Zhou, F. Miao, T. Zhai, *Nat. Electron.* **2022**, *5*, 248.
[16] D. Wu, Y. Wang, L. Zeng, C. Jia, E. Wu, T. Xu, Z. Shi, Y. Tian, X. Li, Y. H. Tsang, *ACS Photonics* **2018**, *5*, 3820.
[17] M. D. Tran, S. G. Lee, S. Jeon, S. T. Kim, H. Kim, V. L. Nguyen, S. Adhikari, S. Woo, H. C. Park, Y. Kim, J. H. Kim, Y. H. Lee, *ACS Nano* **2020**, *14*, 13905.
[18] J. Feldmann, N. Youngblood, M. Karpov, H. Gehring, X. Li, M. Stappers, M. L.e Gallo, X. Fu, A. Lukashchuk, A. S. Raja, J. Liu, C. D. Wright, A. Sebastian, T. J. Kippenberg, W. H. P. Pernice, H. Bhaskaran, *Nature* **2021**, *589*, 52.
[19] F. Wu, Q. Li, P. Wang, H. Xia, Z. Wang, Y. Wang, M. Luo, L. Chen, F. Chen, J. Miao, X. Chen, W. Lu, C. Shan, A. Pan, X. Wu, W. Ren, D. Jariwala, W. Hu, *Nat. Commun.* **2019**, *10*, 4663.
[20] Z. Zhang, P. Lin, Q. Liao, Z. Kang, H. Si, Y. Zhang, *Adv. Mater.* **2019**, *31*, 1806411.
[21] H. Wang, Z. Li, D. Li, P. Chen, L. Pi, X. Zhou, T. Zhai, *Adv. Funct. Mater.* **2021**, *31*, 2103106.
[22] V. K. Dat, C. Hong, M. D. Tran, T. K. Chau, V. D. Do, T. T. Tran, M. C. Nguyen, H. P. Duong, S. Oh, W. J. Yu, J. Kim, J. H. Kim, *Adv. Electron. Mater.* **2024**, *10*, 2300517.
[23] M. D. Tran, H. Kim, J. S. Kim, M. H. Doan, T. K. Chau, Q. A. Vu, J. H. Kim, Y. H. Lee, *Adv. Mater.* **2019**, *31*, 1807075.
[24] C. Hong, S. Oh, V. K. Dat, S. Pak, S. Cha, K. H. Ko, G. M. Choi, T. Low, S. H. Oh, J. H. Kim, *Light. Sci. Appl.* **2023**, *12*, 280.
[25] L. Yin, R. Cheng, J. Ding, J. Jiang, Y. Hou, X. Feng, Y. Wen, J. He, *ACS Nano* **2024**, *18*, 7739.
[26] C. Hong, V. K. Dat, M. C. Nguyen, W. J. Yu, J. H. Kim, *Adv. Funct. Mater.* **2024**, *34*, 2407821.
[27] Y. Wang, W. Zhai, Y. Ren, Q. Zhang, Y. Yao, S. Li, Q. Yang, X. Zhou, Z. Li, B. Chi, J. Liang, Z. He, L. Gu, H. Zhang, *Adv. Mater.* **2023**, 2307269.
[28] Y. T. Lee, P. J. Jeon, J. H. Han, J. Ahn, H. S. Lee, J. Y. Lim, W. K. Choi, J. D. Song, M. C. Park, S. Im, D. K. Hwang, *Adv. Funct. Mater.* **2017**, *27*, 1703822.
[29] W. Wang, W. Wang, Y. Meng, Q. Quan, Z. Lai, D. Li, P. Xie, S. Yip, X. Kang, X. Bu, D. Chen, C. Liu, J. C. Ho, *ACS Nano* **2022**, *16*, 11036.
[30] J. You, Z. Jin, Y. Li, T. Kang, K. Zhang, W. Wang, M. Xu, Z. Gao, J. Wang, J. K. Kim, Z. Luo, *Adv. Funct. Mater.* **2023**, *34*, 2311134.
[31] Y. Zhang, X. Yang, Y. Dai, W. Yu, L. Yang, J. Zhang, Q. Yu, Z. Dong, L. Huang, C. Chen, X. Hou, X. Wang, J. Li, K. Zhang, *ACS Nano* **2023**, *17*, 8743.
[32] G. Konstantatos, M. Badioli, L. Gaudreau, J. Osmond, M. Bernechea, F. P. Garcia de Arquer, F. Gatti, F. H. Koppens, *Nat. Nanotechnol.* **2012**, *7*, 363.
[33] W. Xin, W. Zhong, Y. Shi, Y. Shi, J. Jing, T. Xu, J. Guo, W. Liu, Y. Li, Z. Liang, X. Xin, J. Cheng, W. Hu, H. Xu, Y. Liu, *Adv. Mater.* **2024**, *36*, 2306772.
[34] M. Peng, Z. Wen, X. Sun, *Adv. Funct. Mater.* **2022**, *33*, 2211548.
[35] V. T. Vu, M. C. Nguyen, W. K. Kim, V. D. Do, V. K. Dat, W. J. Yu, *Small Struct.* **2024**, *5*, 2300401.
[36] Z. Li, T. Yan, X. Fang, *Nat. Rev. Mater.* **2023**, *8*, 587.
[37] X. Hu, X. Li, G. Li, T. Ji, F. Ai, J. Wu, E. Ha, J. Hu, *Adv. Funct. Mater.* **2021**, *31*, 2011284.
[38] Z. Li, T. Yan, X. Fang, *Nat. Rev. Mater.* **2023**, *8*, 587.
[39] P. Yu, Q. Zeng, C. Zhu, L. Zhou, W. Zhao, J. Tong, Z. Liu, G. Yang, *Adv. Mater.* **2021**, *33*, 2005607.
[40] D. Li, C. Lan, A. Manikandan, S. Yip, Z. Zhou, X. Liang, L. Shu, Y. L. Chueh, N. Han, J. C. Ho, *Nat. Commun.* **2019**, *10*, 1664.
[41] B. J. Jeong, K. H. Choi, J. Jeon, S. O. Yoon, Y. K. Chung, D. Sung, S. Chae, B. J. Kim, S. Oh, S. H. Lee, C. Woo, T. Y. Kim, J. Ahn, J. H. Lee, J. Huh, H. K. Yu, J. Y. Choi, *Adv. Funct. Mater.* **2021**, *32*, 2108104.
[42] B. J. Jeong, B. Lee, K. H. Choi, D. Sung, S. Ghods, J. Lee, J. Jeon, S. Cho, S. H. Lee, B. J. Kim, S. I. Kim, J. Huh, H. K. Yu, J. H. Lee, J. Y. Choi, *Nano. Lett.* **2023**, *23*, 6269.
[43] S. Ke, J. Zhou, K. V. Larionov, A. Zhu, Y. Li, H. Zhang, Y. Yang, X. Zhu, L. Li, P. B. Sorokin, M. Tian, W. Gao, X. Liu, *Adv. Opt. Mater.* **2023**, *11*, 2300593.
[44] I. J. Chen, S. Limpert, W. Metaferia, C. Thelander, L. Samuelson, F. Capasso, A. M. Burke, H. Linke, *Nano. Lett.* **2020**, *20*, 4064.
[45] K. K. Paul, J.-H. Kim, Y. H. Lee, *Nat. Rev. Phys.* **2021**, *3*, 178.
[46] T. D. Nguyen, J. Jiang, B. Song, M. D. Tran, W. Choi, J. H. Kim, Y. M. Kim, D. L. Duong, Y. H. Lee, *Adv. Sci.* **2021**, *8*, 2102911.
[47] H. Fang, W. Hu, *Adv. Sci.* **2017**, *4*, 1700323.
[48] C. Hong, Y. Tao, V. K. Dat, J.-H. Kim, *npj Flex. Electron.* **2025**, *9*, 13.
[49] Y. Dong, M. M. Yang, M. Yoshii, S. Matsuoka, S. Kitamura, T. Hasegawa, N. Ogawa, T. Morimoto, T. Ideue, Y. Iwasa, *Nat. Nanotechnol.* **2023**, *18*, 36.
[50] M. G. Uddin, S. Das, A. M. Shafi, L. Wang, X. Cui, F. Nigmatulin, F. Ahmed, A. C. Liapis, W. Cai, Z. Yang, H. Lipsanen, T. Hasan, H. H. Yoon, Z. Sun, *Nat. Commun.* **2024**, *15*, 571.
[51] W. Deng, Z. Zheng, J. Li, R. Zhou, X. Chen, D. Zhang, Y. Lu, C. Wang, C. You, S. Li, L. Sun, Y. Wu, X. Li, B. An, Z. Liu, Q. J. Wang, X. Duan, Y. Zhang, *Nat. Commun.* **2022**, *13*, 4627.
[52] X. Xu, Z. Han, Y. Zou, J. Li, Y. Gu, D. Hu, Y. He, J. Liu, D. Yu, F. Cao, H. Zeng, *Adv. Mater.* **2022**, *34*, 2108408.
[53] H. H. Yoon, H. A. Fernandez, F. Nigmatulin, W. Cai, Z. Yang, H. Cui, F. Ahmed, X. Cui, M. G. Uddin, E. D. Minot, H. Lipsanen, K. Kim, P. Hakonen, T. Hasan, Z. Sun, *Science* **2022**, *378*, 296.
[54] Signal and Image Processing Institute (USC-SIPI) Image Database https://sipi.usc.edu/database/ (accessed: March 2024)